Frequency-Domain In-Vehicle UWB Channel Modeling

Aniruddha Chandra,*Member,IEEE,* Aleš Prokeš, Pavel Kukolev, Tomáš Mikulášek, Thomas Zemen,*Senior Member,IEEE,* and Christoph F. Mecklenbräuker,*Senior Member,IEEE*

***Abstract*—The aim of this article is to present a simple but robust model characterizing the frequency dependent transfer function of an in-vehicle ultra-wide-band channel. A large number of transfer functions spanning the ultra-wide-band (3 GHz to 11 GHz) are recorded inside the passenger compartment of a four seated sedan car. It is found that the complex transfer function can be decomposed into two terms, the first one being a real valued long term trend that characterizes frequency dependency with a power law, and the second term forms a complex correlative discrete series which may be represented via an autoregressive model. An exhaustive simulation framework is laid out based on empirical equations characterizing trend parameters and autoregressive process coefficients. The simulation of the transfer function is straightforward as it involves only a handful of variables, yet it is in good agreement with the actual measured data. The proposed model is further validated by comparing different channel parameters, such as coherence bandwidth, power delay profile, and root mean square delay spread, obtained from the raw and the synthetic data sets. It is also shown how the model can be compared with existing time-domain Saleh-Valenzuela influenced models and the related IEEE standards.**

***Index Terms*—Ultra wide band, autoregressive model, transfer function, frequency dependency, intra-vehicle.**

I. Introduction

CONNECTED-VEHICLES represents one of the key features of an intelligent transportation system (ITS) [1], [2] and such vehicles are expected to play a vital role in information and communication technology (ICT) infrastructure in urbanized regions [3]. So far, the related research has been dominantly focused towards design and development of wireless links for vehicle-to-vehicle and vehicle-to-infrastructure scenarios [4]. An IEEE standard, 802.11p [5], has also been devised for the purpose and communication devices conforming to the standard is being implemented in personal [6] and public transport [7] vehicles. For an comprehensive realization of the connected-vehicles vision, it is also important to consider the links inside a vehicle. It is well known that intra-vehicular wireless communication helps in increasing fuel efficiency by reducing the overall wiring harness and simplify manufacturing and maintenance of vehicles [8]. A typical modern day car houses hundreds of sensors [9] connected to an on-board unit (OBU) for monitoring safety, diagnostics, and convenience. The OBU can also provide last-hop wireless connectivity to personal electronic gadgets (smartphone, tablet, laptop etc.) opening up a plethora of new possibilities. On one hand, it will be possible to obtain user-defined real-time multimedia streaming for navigational or recreational purposes [10]. On the other hand, locating people and device would trigger new applications such as smart airbag control [11] or profile restriction of handheld devices [12]. However, these demands can only be met if the wireless technology provides a high bandwidth and assists in precise localization.

Ultra wide band (UWB) has established itself as a preferred technology for high-data-rate, short-range, low-power communication with centimeter-level localization accuracy. Extensive UWB measurement campaigns resulted in a series of channel models [13], [14]. Nevertheless, location specific information is a prerequisite for formulating realistic and reproducible channel models, especially in vehicular environments [15]. In order to determine the feasibility of UWB implementation in small personalized vehicles a number of UWB link measurements in passenger cars have been carried out [16]–[21]. Due to its large dynamic range, a vector network analyzer (VNA), is often preferred for such measurements. The two requirements for VNA based setups: transmitter (Tx) and the receiver (Rx) antennas should be within cable length, and the channel should be static, are satisfied for in-car sounding experiments.

Although the raw data obtained from a VNA is available in the frequency domain, most of the intra vehicular channel modeling efforts [17] are concentrated towards the time domain, with the most popular method being utilization of the Saleh-Valenzuela (S-V) model [14], [22]. The process involves inverse fast Fourier transform (IFFT) followed by certain kind of windowing (Hamming, Hanning, Blackman etc.). A series of S-V model parameters (decay and arrival rate of clusters and rays within each cluster) are found next. The method

Manuscript received October 01, 2015; revised February 03, 2016.

This work was supported by the SoMoPro II programme, Project No. 3SGA5720 *Localization via UWB*, co-financed by the People Programme (Marie Curie action) of the Seventh Framework Programme (FP7) of EU according to the REA Grant Agreement No. 291782 and by the South-Moravian Region. The research is further co-financed by the Czech Science Foundation, Project No. 13-38735S *Research into wireless channels for intra-vehicle communication and positioning*, and by Czech Ministry of Education in frame of National Sustainability Program under grant LO1401. For research, infrastructure of the SIX Center was used.

Part of this research has been presented in the 19th International Conference on Circuits, Systems, Communications and Computers (CSCC 2015).

A. Chandra, A. Prokeš, P. Kukolev, and T. Mikulášek are with the Department of Radio Electronics, Brno University of Technology, 61600 Brno, Czech Republic (e-mail: aniruddha.chandra@ieee.org; prokes@feec.vutbr.cz; xkukol01@stud.feec.vutbr.cz; mikulasekt@feec.vutbr.cz).

T. Zemen is with the Digital Safety and Security Department, AIT Austrian Institute of Technology, 1220 Vienna, Austria (e-mail: thomas.zemen@ait.ac.at).

C. F. Mecklenbräuker is with the Institute of Telecommunications, Technische Universität Wien, 1040 Vienna, Austria (e-mail: cfm@nt.tuwien.ac.at).

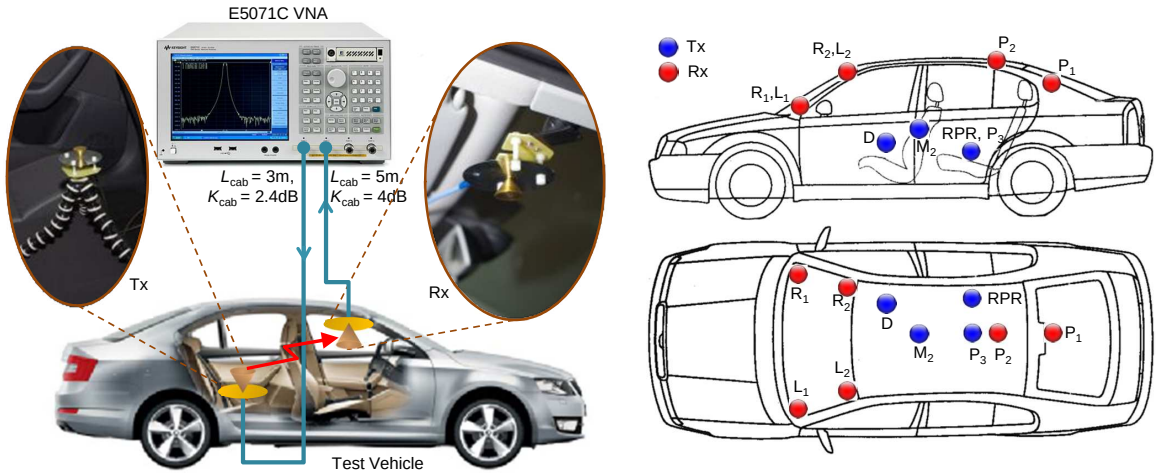

Fig. 1. Measurement setup (left) and antenna placement inside car (right).
Tx legends - D: driver, RPR: rear passenger on right, P_3: middle of backseat, M_2: midpoint between two front seats.
Rx legends - L_1: left dashboard, R_1: right dashboard, L_2: left windshield, R_2: right windshield, P_1 and P_2: positions at rear part of the ceiling.

involves cluster identification which is ambiguous, requires a lot of parameters, and introduce distortion due to IFFT and windowing. If a model can be developed directly from the frequency domain data that requires only a handful of parameters for characterization, simulation of the intra-vehicle channels would be simpler and more reliable helping designers of various in-vehicle communication and localization systems.

This paper aims at analyzing the channel transfer function (CTF) of in-car UWB channels in the frequency domain. Our model is simple to implement as it is not computationally intensive like models using ray tracing based simulation [23] or propagation graphs [24]. In spite of that, the proposed model achieves a good degree of accuracy. Specifically our contributions are the following:

- We propose an autoregressive (AR) process for channel frequency transfer function modeling of UWB links in a *car*. To the best of our knowledge, this has not been attempted so far. Undoubtedly, AR models are a very mature topic that has been used since many decades but it has been applied to UWB propagation in large passenger vehicles like planes [25]. More importantly, we demonstrate that the AR process should be applied *after removing the long term frequency trend* from the transfer function. The method is also different from earlier work on characterizing the frequency dependency of intra-vehicular wireless channels, such as [26], where only simple models of large scale frequency variation were reported.
- Appropriate long term trend equations, in the form of power law, are proposed. Next, assuming that passenger occupancy affects only the long term trend parameters, we find empirical relations to predict the change in such parameters when the number of passengers are changed. Results from an extensive measurement campaign on UWB propagation inside passenger compartment of a car is used for the purpose.
- For the short term trend modeled with a AR process, we propose a simple set of equations to predict the process coefficients. The method is simpler than those presented in [27], [28] which requires the characterization of initial conditions.
- A simple step by step process is demonstrated for simulating the overall CTF. Simulated outputs are validated against the real life measurements.

The rest of the paper is organized as follows. The next section provides description of the experimental setup. The detailed modeling for long term and short term frequency variations are presented in Section III and Section IV, respectively. The overall simulation framework is presented in Section V. This section also includes output of the model and subsequent validation through different quantities of interest. Finally, Section VI concludes the paper.

II. Experimental Setup

A set of intra-vehicular channel transfer functions (CTFs) were measured with a four port VNA (model: Agilent E5071C). The vehicle under test is a four seater Skoda sedan (model: Octavia III 1.8 TSI), with dimensions: 4.659 m (length) $\times$ 1.814 m (width) $\times$ 1.462 m (height), parked at the sixth basement floor in an underground garage. The experimental setup is detailed in Fig. 1. Port 1 and port 2 of the VNA were connected to the transmitter (Tx) and the receiver (Rx) antennas, respectively, and the scattering parameter, s_{21}, which signifies the forward voltage gain approximates the CTF, $H(f)$. Tx and Rx antennas are connected to the VNA via phase stable coaxial cables. The cable length (L_{cab}) and cable attenuations (K_{cab}) were measured, and are indicated in Fig. 1.

The Tx and Rx antenna positions inside the passenger compartment are also shown in Fig. 1. The different configurations ensure both line-of-sight (LoS) and non-line-of-sight (nLoS) propagation conditions. In order to test the effect of passenger occupancy, we varied the number of passengers (n_P) from zero to two at each location. The shadowing in nLoS cases is caused by the seats and the persons sitting inside the vehicle.

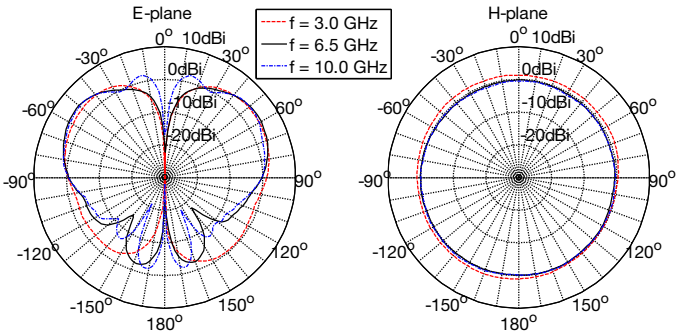

Fig. 2. Measured gain pattern of the conical monopole antennas in E-plane (left-hand side) and H-plane (right-hand side).

A pair of identical conical monopole antennas were used as Tx and Rx and it can be observed from the corresponding measured radiation pattern shown in Fig. 2 that the azimuth plane radiation is circular and invariant within the desired frequency band (3-10 GHz). Variations in the elevation plane do not pose serious concerns because in most of the measurements the Tx-Rx line is contained in the main lobe. In general, the monopole conical antennas have a low radar cross-section and provide a low voltage standing wave ratio [29]. Further, the gain of a conical monopole antenna in the frequency range 3-11 GHz is almost constant [30]. Thus it is possible to analyze the measured wideband CTF without considering the effect of frequency on antennas.

TABLE I
VNA PARAMETERS FOR UWB MEASUREMENT

Parameter	Description	Value
P_{VNA}	Transmit power	5 dBm
$\mathrm{BW}_{\mathrm{IF}}$	IF filter bandwidth	100 Hz
f_L	Start frequency	3 GHz
f_H	Stop frequency	11 GHz
BW	Bandwidth	8 GHz
N_{VNA}	Number of points	801
f_s	Frequency step size	10 MHz
t_{res}	Time resolution	125 ps
$L_{\mathrm{CIR}(t)}$	Maximum CIR length (time)	100 ns
d_{res}	Distance resolution	3.75 cm
$L_{\mathrm{CIR}(d)}$	Maximum CIR length (distance)	30 m
$H_{\mathrm{fil}}(f)$	Windowing for IFFT	Blackman

The frequency-domain measurement parameters are summarized in Table I. The maximum value of the output transmit power of the VNA (P_{VNA}) and the minimum measurable power (or noise floor) together define the system's dynamic range. A trade-off between noise floor and sweep speed may be attained by controlling the intermediate frequency filter bandwidth ($\mathrm{BW}_{\mathrm{IF}}$) and/or averaging. In our experiment, the frequency range between the start frequency, $f_L = 3$ GHz, and the stop frequency, $f_H = 11$ GHz, is swept. The number of discrete frequency tones generated by the VNA in the range, $N_{\mathrm{VNA}} = 801$, and the bandwidth, $\mathrm{BW} = f_H - f_L = 8$ GHz, determine the frequency resolution as per the relation, $f_s = (f_H - f_L)/(N_{\mathrm{VNA}} - 1) = \mathrm{BW}/(N_{\mathrm{VNA}} - 1)$. Further, the sweeping bandwidth sets the time resolution, $t_{\mathrm{res}} = 1/\mathrm{BW}$, i.e. the minimum time between samples in the time-domain channel impulse response (CIR) function obtained after inverse fast Fourier transform (IFFT), whereas the frequency step size (f_s) characterizes the maximum observable delay spread, $L_{\mathrm{CIR}(t)} = 1/f_s$, i.e. the maximum time delay until the multipath components (MPCs) are observed. The distance resolution, $d_{\mathrm{res}} = c \cdot t_{\mathrm{res}} = c/\mathrm{BW}$, refers to the length an electromagnetic wave can propagate in free space ($c = 3 \times 10^8 \mathrm{m/s}$) during time t_{res} and the corresponding distance range is $L_{\mathrm{CIR}(d)} = c/f_s$.

The CIR obtained with VNA through the IFFT operation can be expressed as, $h_{\mathrm{VNA}}(t) = h(t) * h_{\mathrm{fil}}(t)$, where $H_{\mathrm{fil}}(f) = \mathcal{F}\{h_{\mathrm{fil}}(\tau)\}$ is the transfer function of the windowing operation. We used the Blackman window which ensures minimum spectral distortion, i.e. high side lobe suppression and reasonable main lobe width [31]. High side lobe suppression is preferred to a narrower main lobe width, because it decreases the probability of unwanted detection of a side lobe as the first arriving ray [32]. However, this feature is crucial for ranging applications and filtering considerations are not important for the basic CTF simulation.

III. Long Term Variations

Let us investigate a typical measured CTF as depicted in Fig. 3. The magnitude of CTF has a overall downward slope with respect to frequency and the first step of our modeling involves separating this long term variation or trend, i.e. we express the complex CTF as

$$H(f) = \tilde{H}(f) \cdot |H(f)|_{\mathrm{trend}} \tag{1}$$

where $\tilde{H}(f)$ denotes the complex short-term variations of the CTF.

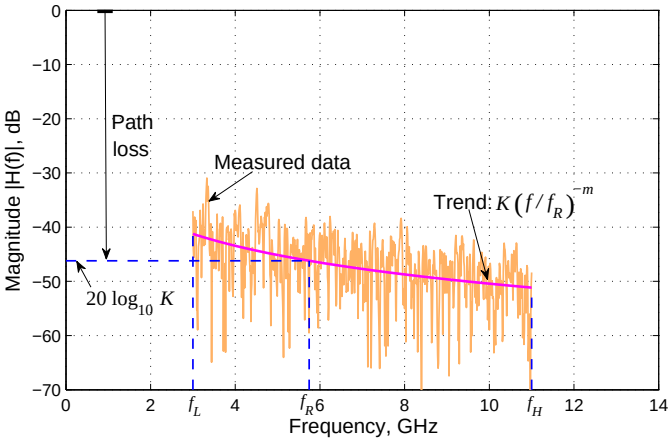

Fig. 3. CTF and estimated trend (Tx position: P_3, Rx position: L_2, and $n_P = 0$).

The well known free space path loss formula suggests that the CTF amplitude is inversely proportional to frequency [33]–[36] and the long term variations can be modeled with a simple power law

$$|H(f)|_{\mathrm{trend}} = K \left(\frac{f}{f_R} \right)^{-m} \tag{2}$$

as devised in [37]. In (2), the parameter K is a proportionality constant and m is a power law exponent. The reference

frequency, $f_R = \sqrt{f_L f_H}$, depends on the lower (f_L) and upper (f_H) bound of the frequency band and is equal to the geometric mean of the bounds. For the current UWB experiment ($f_L = 3$ GHz, $f_H = 11$ GHz), $f_R = 5.74$ GHz.

There also exists another exponential model for frequency dependence in ultrawide band [38]

$$20 \cdot \log_{10} |H(f)|_{\text{trend}} = K' \cdot \exp(-m' f) \tag{3}$$

In [39], it was shown that the root mean square error for both the trends given by (2) and (3) are comparable for the whole set of experimental data. However, we considered the power law over the exponential one due to three factors; first, the power law has a sound mathematical basis, second, the majority of the authors recommended the former over the later, and third, the power equation is currently adopted in IEEE 802.15.4a UWB standard documentation [40].

In Fig. 3 the estimated trend with least mean square error fitting for a particular data set is shown. The parameter values in an empty car ($n_P = 0$) for all different antenna locations are listed in Table II.

TABLE II
PARAMETER VALUES OF THE FREQUENCY TREND FOR DIFFERENT TX AND RX ANTENNA POSITIONS (MARKINGS ARE AS PER FIGURE 1)

Tx	Rx	Tx-Rx distance in m	Path loss in dB $(-20\log_{10} K)$	Power law exponent (m)	Remark (LoS / nLoS)
D	R_2	0.56	40.4402	0.6988	LoS
P_3	P_2	0.60	41.9495	0.7583	LoS
RPR	P_2	0.70	41.0768	1.2355	LoS
M_2	L_2	0.73	39.9511	0.4913	LoS
M_2	R_2	0.76	39.2481	0.6145	LoS
P_3	P_1	0.76	39.6790	1.1910	LoS
RPR	P_1	0.84	41.3834	0.8015	LoS
D	R_1	0.85	44.9526	0.9257	LoS
M_2	P_2	0.87	40.0627	0.9788	LoS
D	L_2	0.97	38.9088	1.2165	LoS
D	L_1	1.16	45.5443	1.1257	LoS
D	P_2	1.23	43.8985	0.9498	nLoS
P_3	L_2	1.23	46.1980	0.8776	nLoS
RPR	R_2	1.25	45.3958	0.9250	nLoS
P_3	R_2	1.28	45.4769	1.1457	nLoS
RPR	L_2	1.44	46.7050	1.2859	nLoS
D	P_1	1.48	46.4266	0.5556	nLoS
RPR	R_1	1.57	47.9343	1.0283	nLoS
P_3	L_1	1.62	48.1986	1.0062	nLoS
P_3	R_1	1.65	48.3114	1.0030	nLoS
RPR	L_1	1.74	49.7412	1.0637	nLoS

A. Characterization of K

A physical interpretation of the parameter K can be derived as hereunder. The path loss (α) of a channel is defined as the ratio of the transmit power to the receiver power (P_t/P_r), and in dB scale it may be written as

$$\alpha = 10\log_{10}\left(\frac{P_t}{P_r}\right) = -20\log_{10}|H(f)| \tag{4}$$

which is obtained by noting that the CTF is the ratio of the channel output to the channel input in the frequency domain, i.e. $P_t/P_r = 1/|H(f)|^2$.

Next, substituting the CTF magnitude trend (instead of the overall CTF magnitude) from (2) in (4), we have

$$\alpha = -20\log_{10} K + 20m \cdot \log_{10}(f/f_R) \tag{5}$$

From (5), it is easy to verify that $\alpha_{f_R} = -20\log_{10} K$. In other words, the path loss at the reference frequency, $\alpha_{f_R} = \alpha(f = f_R)$, is equal to the parameter K in dB scale with a negative sign (PL is a positive quantity). The concept is graphically explained in Fig. 3 and we have listed α_{f_R} (rather than K) in Table II as it is more intuitive to deal with the path loss data.

To avoid any confusion, we would like to state that in majority of literature [41] the path loss data is computed from VNA data by averaging the inverse of squared CTF over the whole frequency range

$$\alpha = 10\log_{10}\left(\frac{1}{N_{\text{VNA}}}\sum_{n=1}^{N_{\text{VNA}}}\frac{1}{|H(f_n)|^2}\right) \tag{6}$$

whereas, in our case, we have computed the long term frequency trend parameters (K and m) for each measurement through finding the best-fitting curve that minimizes the sum of the squares of the residuals. This is followed by calculation of the path loss at the reference frequency (α_{f_R}) from K.

After establishing the relation of K with path loss, we investigate the effect of propagation distance on K (or to be more specific, on α_{f_R}). It is possible to relate the path loss data with the Tx-Rx separation through the following equation [42]

$$\alpha_{f_R} = \alpha_{f_R}(d_0) + 10\gamma\log_{10}\left(\frac{d}{d_0}\right) + \chi \tag{7}$$

where $\alpha_{f_R}(d_0)$ is the path loss at $d_0 = 1$ m [1], γ is the path loss exponent and $\chi \sim \mathcal{N}(0, \sigma_\chi^2)$ is a normal distributed random variable which accounts for the log-normal shadowing. A least square linear regression fitting between computed α_{f_R} values across all the measurements and the corresponding distances (d) gives us the parameters in (7), for both LoS and nLoS conditions, which are mentioned in Table III. From the residuals of the regression analysis the log-normality of the shadowing was also verified via normal probability plots. However, the regression lines and probability plots are omitted here (as well as in all the following regression analyses in this paper) for brevity.

TABLE III
PATH LOSS PARAMETERS FOR THE LOS AND THE NLOS CASES

Scenario	Path loss intercept, dB $(\alpha_{f_R}(d_0))$	Path loss exponent (γ)	Shadowing variance, dB (σ_χ^2)
LoS	42.1737	0.9198	2.0387
nLoS	42.4952	2.7559	0.6262

[1] Although it is a common practice to consider the smallest possible Tx-Rx separation, which is 0.56 m, as the reference distance, here we followed a general recommendation to consider $d_0 = 1$ m for indoor environments. It is highly likely that path loss values for such a common reference distance is available for other environments, and comparison with values in Table III would be more straightforward.

B. Characterization of m

For indoor UWB propagation, a value range of $0.8 < m < 1.4$ was reported earlier [43]. The m values in Table II roughly follows the limits. Our results are also consistent with previous measurements inside car compartment [44] where a $1/f^2$ decay was observed in the power spectra which translates to the $1/f$ decay in the amplitude domain. The experiments conducted at other parts (e.g. under the chasis [45]) of the vehicle with less favourable propagation modes results in a higher m.

It is interesting to note that the values of m for the current experiments are uniformly distributed and do not depend on the Tx-Rx gap. A simple averaging is thus sufficient to model the power law exponent. The average values obtained for LoS and nLoS cases are as follows

$$< m >= \begin{cases} 0.9125 & : \text{LoS} \\ 0.9841 & : \text{nLoS} \end{cases} \tag{8}$$

C. Effect of passenger occupancy

As mentioned in Section II, we have repeated our measurements for each antenna combination by varying the passenger occupancy. Although the maximum capacity of the car is four, one location was always occupied by the Tx antenna and the tripod on which it was fixed, and the other location was not accessible due to connecting cables. Thus we could test each location with minimum zero and maximum two passengers.

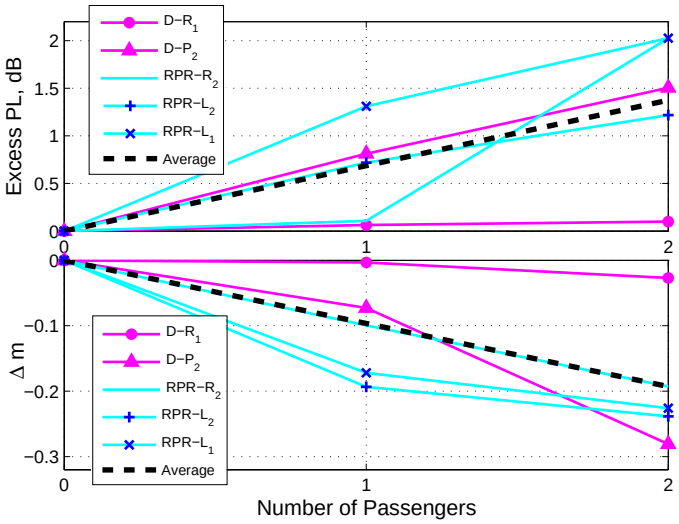

Fig. 4. Effect of passenger on PL at reference frequency and on the PL trend exponent.

The effect of number of passengers on PL and exponent value are shown in Fig. 4. For both the figures we have only plotted the change in parameter values, i.e. excess PL $= \alpha_{f_R}(n_P) - \alpha_{f_R}$ and $\Delta m = m(n_P) - m$, with respect to number of passengers (n_P). While the PL increases due to additional shadowing, the power law exponent lowers with more passengers making the CTF flatter. This phenomena was earlier observed in [26, (2)] for in-car experiments where the exponent is quantified with a large negative slope with respect to frequency and was demonstrated for indoor office environments [46, Fig. 5(b)] where the PL coefficient decreases with more number of people in the room when the receiver is placed close to occupants. Although the human tissue exhibits a constant decrease in permittivity with frequency [47], the flattening of CTF is perhaps accounted to the absence of rich scattering multipath components.

Plots in Fig. 4 for different Tx locations are depicted with separate colours (magenta for Tx at D and cyan for Tx at RPR), but it was hard to find any specific correlation of the trends with the antenna positions.

A simple averaging of the upward trends (shown with black dotted line in Fig. 4) across different locations enables us to express the PL with passengers in the following manner

$$\alpha_{f_R}(n_P) = \alpha_{f_R} + 0.6876 \times n_P \quad ; \; n_P = 0, 1, 2 \tag{9}$$

whereas for the exponent, which is monotonically decreasing, the following average equation is found to be valid

$$m(n_P) = m - 0.0965 \times n_P \quad ; \; n_P = 0, 1, 2 \tag{10}$$

IV. Short Term Variations

After finding out the long term trends, we proceed with the characterization of the normalized CTF, namely, $\tilde{H}(f)$. Autoregressive or AR modeling belongs to the class of parametric spectral estimation and as the variations of $\tilde{H}(f)$ resembles a correlated series with low peaks and deep fades, an AR model is preferred [48] over moving average (MA) or hybrid ARMA models. An AR model for wideband indoor radio propagation was first presented in [49], and later applied to UWB channel modeling in [41] for indoor scenarios and in [50] for underground mines.

The normalized CTF under a q order AR process assumption may be mathematically expressed as

$$\tilde{H}(f_n) = \sum_{k=1}^{q} a_k \tilde{H}(f_{n-k}) + \xi_n \tag{11}$$

where, f_n; $n = 1, 2, \cdots N_{\text{VNA}}$, is the nth discrete frequency in the CTF vector, a_k; $k = 1, 2, \cdots q$, are the complex AR process coefficients, and ξ_n is the nth sample of a complex Gaussian process with variance σ_ξ^2. A z-transform, $\tilde{H}(z) = \sum_n \tilde{H}(f_n) z^{-n}$, allows us to view the CTF as the output of a all pole linear infinite impulse response (IIR) filter with transfer function, $\mathcal{G}(z) = \tilde{H}(z)/\xi(z)$, excited by white Gaussian noise [49], i.e.

$$\mathcal{G}(z) = \frac{1}{1 - \sum_{k=1}^{q} a_k z^{-k}} = \prod_{k=1}^{q} \frac{1}{1 - p_k z^{-k}} \tag{12}$$

The equivalent filter structure is presented in Fig. 5.

The poles (p_k) and the noise variance (σ_ξ^2) are found by solving the Yule-Walker equations [51] which obtains the least square error. The solution involves converting (11) to the autocorrelation domain

$$\begin{aligned} R_{\tilde{H}\tilde{H}}(j) &= \mathcal{E}\left\{\tilde{H}(f_n)\tilde{H}(f_{n-j})\right\} \\ &= \sum_{k=1}^{q} a_k R_{\tilde{H}\tilde{H}}(j-k) + \sigma_\xi^2 \delta(j) \end{aligned} \tag{13}$$

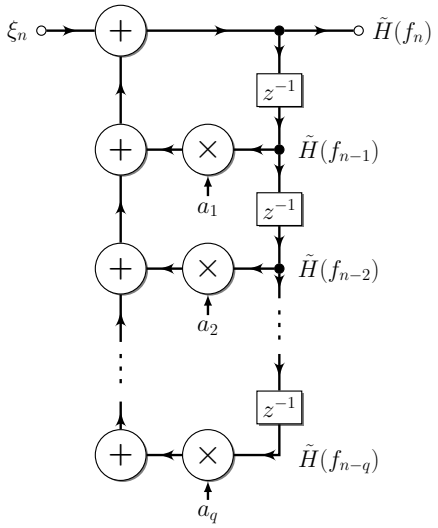

Fig. 5. Direct form filter implementation of the AR process for short term variations.

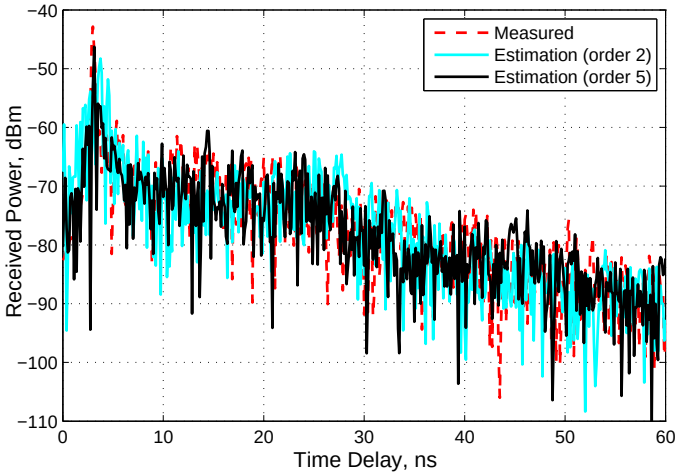

Fig. 6. Measured and estimated PDPs with two different order AR processses. Tx position: P_3, Rx position: P_1, and $n_P = 0$.

with $\mathcal{E}\{\cdot\}$ denoting the expectation operator and $\delta(\cdot)$ is delta function, and then solving for the process coefficients

$$R_{\tilde{H}\tilde{H}}(-j) - \sum_{k=1}^{q} a_k R_{\tilde{H}\tilde{H}}(k-j) = 0 \; ; \; j > 0 \tag{14}$$

as well as the noise variance

$$\sigma_\xi^2 = R_{\tilde{H}\tilde{H}}(0) - \sum_{k=1}^{q} a_k R_{\tilde{H}\tilde{H}}(k) \tag{15}$$

It should be noted here that our model does not require initial conditions of the IIR filter and thereby reduces the complexity of the models compared to those presented in [27], [28].

A. AR process order selection

In general, higher order AR process provides better estimation but with diminishing returns as q increases, and there exists a tradeoff between accuracy and complexity. Although a second order $(q = 2)$ AR process was sufficient for indoor [41] and underground mines [50], we propose a fifth order $(q = 5)$ process as the car compartment exhibits multiple overlapped clusters. The following figure, Fig. 6, shows the result of power delay profile (PDP) estimations with a 2nd order and with a 5th order AR process (refer to Section V for more details on PDP). One may notice that even for a direct LoS path (Tx: P_3, Rx: P_1), the estimation with 2nd order process results in incorrect delay calculation for the first arriving path or the peak. The problem is more prominent for the nLoS situations.

The pole amplitudes, pole angles, and input noise variances for the entire measurement set is listed in Table IV considering a fifth order AR process estimation of the CTF short term variations.

In [49], the AR process order estimation was carried out by comparing the cumulative distribution function (CDF) of the 3 dB width of the frequency correlation function and CDF of the root mean square delay spread (for definitions, refer to Section V). A mathematically rigorous method is, however, to choose the process order through Akaikes information criterion (AIC) [41], [52] or minimum description length (MDL) [53], [54]. We have refrained from such analysis as it is out of scope of the present paper.

B. Characterization of input noise

The AR process is driven by, $\xi_n \sim \mathcal{CN}(0, \sigma_\xi^2)$, a complex zero mean Gaussian noise, and looking at the entries in Table IV, one can find that its variance increases with Tx-Rx separation. A linear regression fitting yields the following empirical relation for the data set obtained

$$\sigma_\xi^2 = 0.0024 + 0.107 \times d \tag{16}$$

where d is the propagation distance in meters. It may be noted that (16) is obtained through fitting across all the values in Table IV without attempting to differentiate between LoS and nLoS cases. This also holds true for the pole parameters which are derived next. Our general assumption is that the LoS/ nLoS conditions affect only the parameters that are associated with the long term variations. This enables us to realize a simulation model with minimum inputs.

C. Characterization of poles

Fig. 7 plots the estimated pole locations for all the different sets of experiments as listed in Table IV. When the poles are sorted in the descending order of their amplitudes, they form distinguished clusters in the complex plane.

Let us analyze the amplitude of the poles first. The pole clusters represent multipath clusters and the amplitudes of the higher order pole clusters shifts away from the unit circle as they contribute lesser power in the overall power delay profile [49]. Fortunately, the amplitudes inside a cluster is fairly constant, and it is possible to approximate the pole amplitudes $(|p_k|; k = 1, 2, \cdots, 5)$ with the mean amplitude value of the cluster

$$< |p_k| >= \begin{cases} 0.9722 & ; \; k = 1 \\ 0.8346 & ; \; k = 2 \\ 0.7343 & ; \; k = 3 \\ 0.6573 & ; \; k = 4 \\ 0.6036 & ; \; k = 5 \end{cases} \tag{17}$$

It was suggested in [50], [55] that the pole angles are related

TABLE IV
PARAMETER VALUES OF AR PROCESS FOR DIFFERENT TX AND RX ANTENNA POSITIONS (MARKINGS ARE AS PER FIGURE 1)

Tx	Rx	Tx-Rx distance in m	Pole amplitudes					Pole angles in radians					Noise variance (σ_ξ^2)	Remark (LoS / nLoS)
			$\lvert p_1\rvert$	$\lvert p_2\rvert$	$\lvert p_3\rvert$	$\lvert p_4\rvert$	$\lvert p_5\rvert$	$\angle p_1$	$\angle p_2$	$\angle p_3$	$\angle p_4$	$\angle p_5$		
D	R_2	0.56	0.9844	0.8416	0.7801	0.6773	0.6357	-0.2578	-0.7162	-1.6014	-2.6323	2.4051	0.0577	LoS
P_3	P_2	0.60	0.9702	0.7738	0.7328	0.7038	0.6145	-0.2121	-0.7477	-1.4538	-2.6015	2.3436	0.1355	LoS
RPR	P_2	0.70	0.9775	0.8328	0.7492	0.6855	0.6211	-0.2378	-0.7358	-1.5814	-2.6406	2.4533	0.0915	LoS
M_2	L_2	0.73	0.9852	0.8352	0.6449	0.6433	0.5530	-0.1959	-0.8360	-1.6695	-2.6379	2.1722	0.0798	LoS
M_2	R_2	0.76	0.9906	0.8641	0.7322	0.6626	0.6188	-0.1874	-0.7961	-1.6229	-2.6254	2.3512	0.0555	LoS
P_3	P_1	0.76	0.9933	0.8116	0.7581	0.6821	0.6174	-0.1956	-0.8318	-1.5776	-2.7156	2.3671	0.0471	LoS
RPR	P_1	0.84	0.9890	0.8290	0.7018	0.6220	0.6133	-0.2179	-0.8231	-1.6998	-2.6755	2.3329	0.0645	LoS
D	R_1	0.85	0.9657	0.8265	0.6984	0.6131	0.6121	-0.3594	-0.8177	-1.7186	-2.6795	2.3108	0.1006	LoS
M_2	P_2	0.87	0.9859	0.8311	0.7548	0.6567	0.5884	-0.2251	-0.8518	-1.6629	-2.7682	2.2132	0.0874	LoS
D	L_2	0.97	0.9894	0.8428	0.7287	0.6151	0.5870	-0.1831	-0.7303	-1.5664	-2.5906	2.4461	0.0519	LoS
D	L_1	1.16	0.9773	0.8230	0.6759	0.5951	0.5223	-0.2676	-0.9072	-1.6699	-2.7820	2.3486	0.1285	LoS
D	P_2	1.23	0.9726	0.8503	0.7354	0.6556	0.6327	-0.3472	-0.8706	-1.7034	-2.7761	2.3318	0.1113	nLoS
P_3	L_2	1.23	0.9503	0.8463	0.7783	0.7037	0.6254	-0.3492	-0.8984	-1.7449	-2.8202	2.1729	0.1919	nLoS
RPR	R_2	1.25	0.9651	0.8026	0.7511	0.6185	0.6168	-0.3666	-0.9281	-1.7241	-2.7201	2.2717	0.1494	nLoS
P_3	R_2	1.28	0.9451	0.8495	0.7673	0.6761	0.5672	-0.3677	-0.9495	-1.7593	-2.8333	2.2411	0.1746	nLoS
RPR	L_2	1.44	0.9587	0.8560	0.7513	0.6569	0.6002	-0.3628	-0.9603	-1.8069	-2.9035	2.2118	0.2095	nLoS
D	P_1	1.48	0.9824	0.8587	0.7287	0.6682	0.6208	-0.3863	-1.0215	-1.8785	-2.8058	2.1533	0.1278	nLoS
RPR	R_1	1.57	0.9512	0.8189	0.7168	0.5949	0.5210	-0.4826	-1.0101	-1.8694	-2.9434	2.0831	0.1535	nLoS
P_3	L_1	1.62	0.9647	0.8424	0.7477	0.6882	0.6629	-0.4598	-1.0232	-1.8182	-2.8841	2.1109	0.1599	nLoS
P_3	R_1	1.65	0.9617	0.8279	0.7153	0.6775	0.6108	-0.4628	-0.9899	-1.9311	-2.8438	2.0392	0.1691	nLoS
RPR	L_1	1.74	0.9555	0.8632	0.7709	0.7080	0.6344	-0.4284	-0.9892	-1.8201	-2.8985	2.0561	0.1946	nLoS

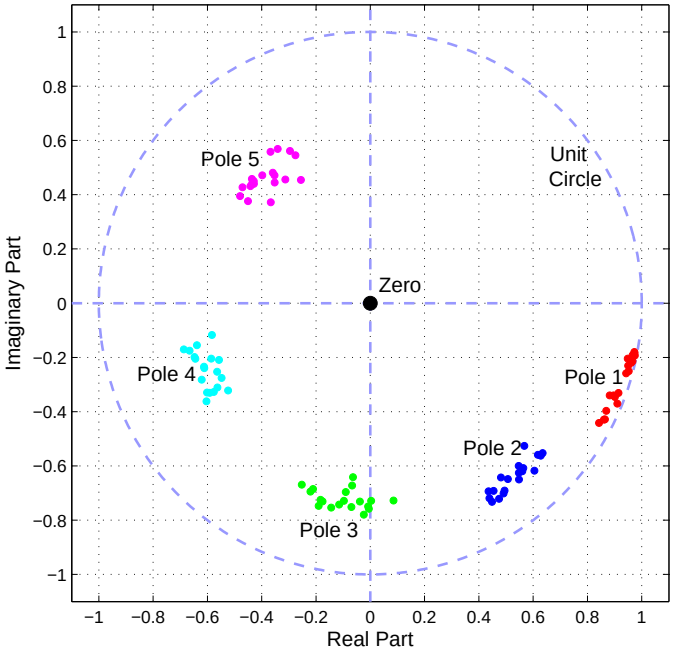

Fig. 7. Complex plane scatter plot of poles for all different experiments.

to the clusters in the following manner

$$\tau_k = -\frac{\theta_k}{2\pi f_s};\ k = 1, 2, \cdots, 5 \tag{18}$$

where τ_k and θ_k are the delay of the kth multipath cluster and angle of the kth pole respectively, while f_s is the frequency step size. During our analysis we found that all the pole angles are linearly dependent on the Tx-Rx gap and (18) overestimates the delays. Therefore we propose the following set of equations to model the pole angles

$$\begin{aligned}
\angle p_1 &= -0.05 - 0.2365 \times d \\
\angle p_2 &= \angle p_1 - 0.5534 - 0.0112 \times d \\
\angle p_3 &= \angle p_2 - 0.7952 - 0.0321 \times d \\
\angle p_4 &= \angle p_3 - 1.0641 + 0.0193 \times d \\
\angle p_5 &= -\angle p_4 + 0.0878 - 0.5246 \times d
\end{aligned} \tag{19}$$

In (19), we have modelled the angles in a successive manner, i.e. the angle of pole 2 depends on pole 1 and so on. The linear regression fitting was operated on the difference of the pole angles to avoid local measurement deviations.

V. SIMULATION AND MODEL VALIDATION

A. Simulation steps

Our proposed simulation model only involves three variables: the Tx-Rx separation (d), number of passengers (n_P), and the propagation condition (LoS/ nLoS). The step-by-step guide to estimate the in-vehicle channel transfer function is as follows:

I Estimate long term variation, $|H(f)|_{\text{trend}}$
- (a) Determine K: Find α_{f_R} from (7) and Table III. The parameter K is related to the path loss as $K = 10^{-\alpha_{f_R}/20}$.
- (b) Determine m: Select m from (8) according to the propagation scenario (LoS/nLoS).
- (c) Passenger effect: Modify K and m value according to the number of passengers following (9) and (10).
- (d) Find trend from (2).

II Estimate short term variation, $\tilde{H}(f)$
- (a) Generate ξ: Find the input noise variance from (16) and generate a complex Gaussian random variable of length N_{VNA} with zero mean and variance σ_ξ^2.

(b) Estimate poles: Approximate the pole amplitudes following (17), and find the phase of each pole in a successive manner as demonstrated in (19).

(c) Filtering: With the poles, construct an all-pole IIR filter as mentioned in (12). Pass ξ through it to get $\tilde{H}(f)$ at output.

III Estimate the CTF, $H(f) = \tilde{H}(f) \cdot |H(f)|_{\text{trend}}$

B. Frequency domain validation

The CTF, $H(f)$, is obtained by combining the long term frequency dependence with the simulated short term AR model based variations. The measured and simulated transfer functions for one particular Tx-Rx pair is shown in Fig. 8.

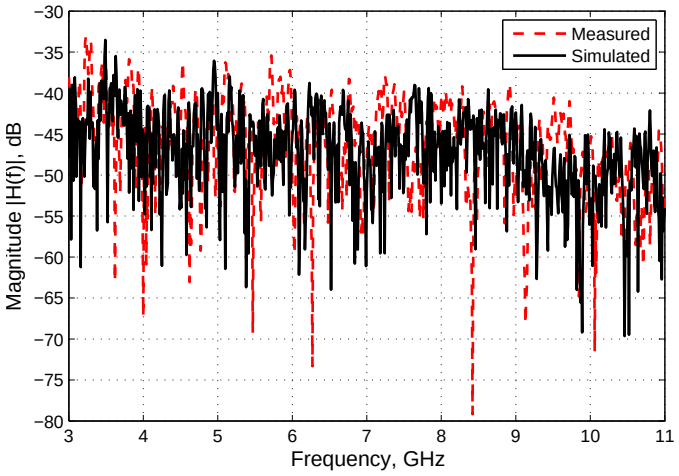

Fig. 8. Measured and simulated CTFs. Tx position: D, Rx position: P_2, and $n_P = 2$ (two passengers on rear seat).

The frequency autocorrelation function (ACF), $R(\Delta f)$, may be found from the channel transfer function as [56]

$$R(\Delta f) = \int_{-\infty}^{\infty} H(f) H^*(f + \Delta f)\, \mathrm{d}f \tag{20}$$

which provides a measure of the frequency selectivity. The range between DC or zero frequency, where normalized ACF attains its peak value of unity, and the frequency where ACF falls to 50% of or 3 dB lower than its peak value, is defined as the coherence bandwidth (BW), B_C. From Fig. 9, it can be seen that the measured and simulated transfer functions manifest almost similar B_C values.

A channel is considered *flat* in the coherence BW interval, i.e. if two different frequencies are separated by more than B_C, the channel exhibits uncorrelated fading at these two frequencies. There is a more direct method available for calculation of coherence BW [57], [58]. However, we computed B_C via the classical approach as the BW spans over only few samples for the current frequency step size (10 MHz), and there might be large approximation errors involved in the direct method.

C. Time domain validation

The complex channel impulse response $h_{\text{VNA}}(t)$ extracted after IFFT operation and windowing is utilized to obtain

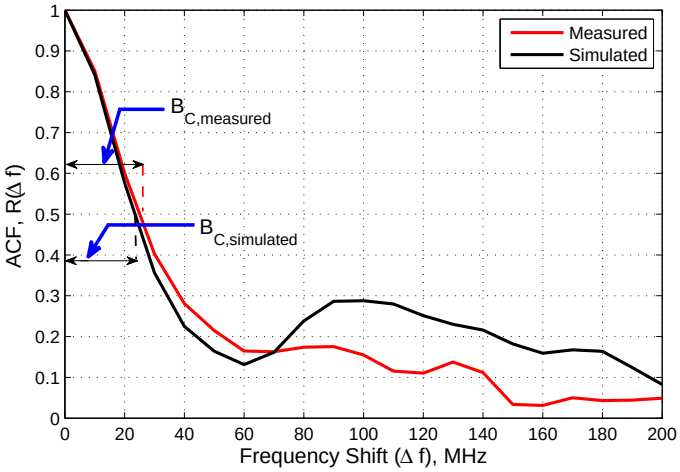

Fig. 9. Comparison of frequency ACF for the CTFs shown in Fig. 8.

the PDP, $\text{PDP}(t) = \mathcal{E}\left\{|h_{\text{VNA}}(t)|^2\right\}$. Fig. 10 shows the comparison of the measured PDP with the simulated PDP, and one can find that there is a close match. A matter of concern is, due to the random inputs, the difference of peaks between consecutive simulation runs can be as high as 10 dB. Fortunately, in most of the cases, the peak locations can still be detected correctly with the simulation. Another concern is the noisy rising edge of the simulated PDP before the first peak which can be suppressed with proper windowing [39], [59] during the IFFT post-processing.

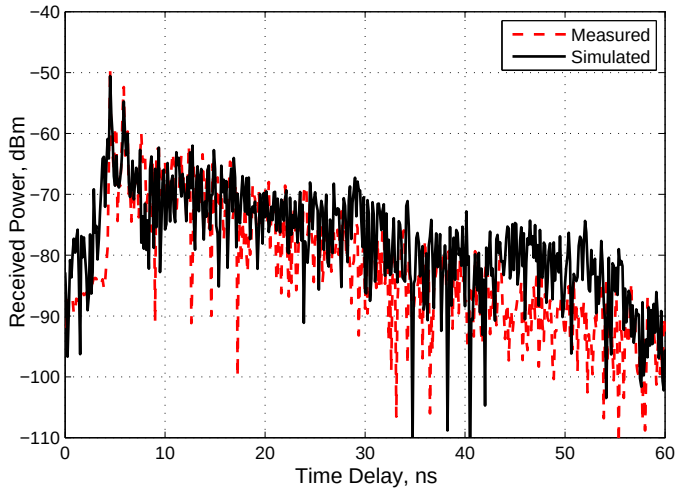

Fig. 10. Measured and simulated PDPs. Tx position: D, Rx position: P_2, and $n_P = 2$ (two passengers on rear seat).

A quantitative comparison between the measured PDP and the simulated PDP can be performed by noting the similarity of the root mean square (RMS) delay spreads obtained for both the delay profiles. RMS delay spread is the second central moment of the PDP

$$\tau_{\text{rms}} = \sqrt{\int_0^{\tau_{\max}} (t - \bar{\tau})^2 \cdot \mathrm{P}_n(t)\, \mathrm{d}t} \tag{21}$$

where $\tau_{\max}$ denotes the maximum excess delay, $\mathrm{P}_n(t) = |h_{\text{VNA}}(t)|^2 / \int_0^{\tau_{\max}} |h_{\text{VNA}}(t)|^2 \mathrm{d}t$ is normalized magnitude

square function, and $\bar{\tau} = \int_0^{\tau_{\max}} t \cdot \mathrm{P}_n(t)\mathrm{d}t$ is the mean excess delay.

For calculating the RMS delays, the rising edge of the PDP is cut off and the time origin is shifted to the time index that corresponds to the peak. This time shifting helps in rendering the delays as excess delays relative to the peak or first arriving path which has a zero delay. Further, only those MPCs having a delay less than $\tau_{\max} = 60$ ns are considered. This step ensures that the truncated PDP does not hit the noise floor. According to the Agilent E5071C VNA data sheet, the noise floor is -120 dBm/Hz. Hence, for a 100Hz IF bandwidth, it is good enough to consider MPCs upto -100 dBm. Finally, the PDPs are normalized so that the peak occurs at 0 dB. The measured RMS delay values are between 5 to 10 ns, and are consistent with time domain measurements of intra-vehicle UWB links [60].

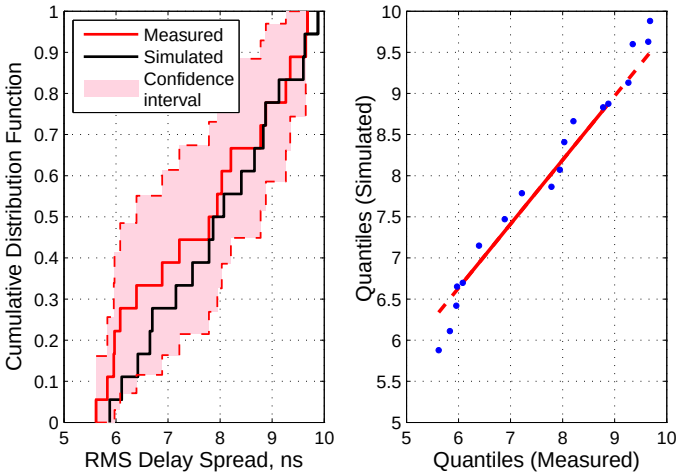

Fig. 11. Measured and simulated RMS delay spreads for empty car - comparison of empirical CDFs (left) and quantile-quantile plot (right).

The simulated PDP matches closely with the measured PDP as the percentage of error

$$\% \text{ error} = \frac{\tau_{\mathrm{rms,simulated}} - \tau_{\mathrm{rms,measured}}}{\tau_{\mathrm{rms,measured}}} \times 100 \qquad (22)$$

is typically 10%, with values ranging between 2% to 30%. The statistical similarity is validated in Fig. 11 which compares the empirical CDFs and it can be clearly seen that the CDF of simulated delay spread is contained within the 95% confidence interval bounds of the CDF of measured delay spread. The degree of similarity between the measured and simulated delay spreads are tested via a two sample Kolmogorov-Smirnov (K-S) test which showed a sufficiently high value, $p = 0.7088$. Linearity of the quantile-quantile plot in Fig. 11 also supports the claim.

The CDF comparison also reveals that probability of smaller delay spread values are more frequent in the measured data compared to the simulated set. This is in line with our observation regarding percentage error which is mostly positive, i.e. the simulated PDP slightly overestimates τ_{rms}, especially for the LoS scenarios with small Tx-Rx separation where the delay spread is low. This is because the simulation model relies on averaging over the entire data set and the local variations for very small d values are not well represented.

D. Comparison with S-V model

Finally, in this sub-section, we show how different Saleh-Valenzuela (S-V) model parameters can be extracted from the proposed frequency-domain model. The S-V model is of considerable interest as the existing time-domain in-vehicle channel models [17]–[21] heavily rely on it. Further, it is also suggested in [18] and [19] to use the IEEE 802.15.3a and IEEE 802.15.4a models, respectively, for simulating in-vehicle UWB propagation. Both these IEEE standards recommend a time-domain model that is based on the basic S-V model.

According to the S-V model, the discrete impulse response of an UWB channel may be expressed as [13]

$$h_{\mathrm{VNA}}(t) = \sum_{n=1}^{N_c} \sum_{m=1}^{N_{r,n}} \beta_{m,n} \exp(j\theta_{m,n}) \delta(t - T_n - \tau_{m,n}) \qquad (23)$$

where N_c is the number of clusters, $N_{r,n}$ is the number of rays in the nth cluster, and T_n is the arrival time of the nth cluster. The magnitude, phase, and additional delay of the mth ray within the nth cluster are given by $\beta_{m,n}$, $\theta_{m,n}$, and $\tau_{m,n}$, respectively. The inter- and intra-cluster exponential decay rates, namely Γ and γ, define the magnitude of individual rays according to

$$\beta_{m,n}^2 = \beta_{1,1}^2 \exp[-(T_n - T_1)/\Gamma] \exp(-\tau_{m,n}/\gamma) \qquad (24)$$

If we assume that both the arrival of clusters and rays within clusters follow independent Poisson processes, the inter-arrival times are exponentially distributed, i.e.

$$\Pr(T_n | T_{n-1}) = \Lambda \exp[-\Lambda(T_n - T_{n-1})] \qquad (25a)$$

$$\Pr(\tau_{m,n} | \tau_{m-1,n}) = \lambda \exp[-\lambda(\tau_{m,n} - \tau_{m-1,n})] \qquad (25b)$$

where $\Pr(\cdot)$ denotes probability. The parameters $1/\Lambda$ and $1/\lambda$ represent the average duration between two consecutive clusters and two consecutive rays within a cluster, respectively.

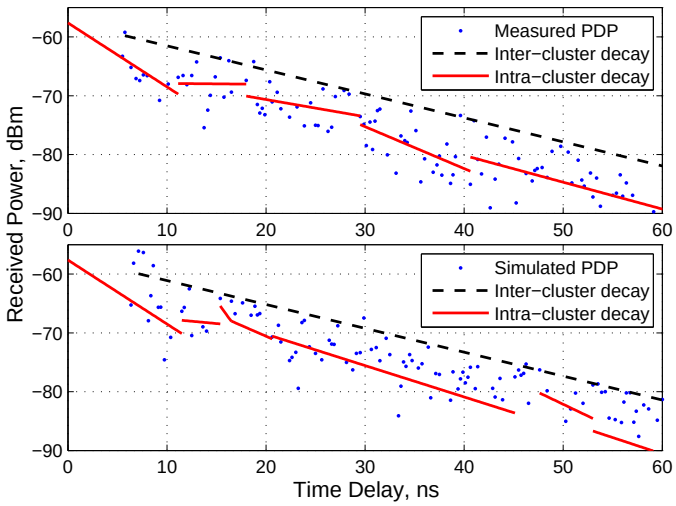

Fig. 12. Cluster identification and S-V model parameter estimation for a typical nLoS scenario. Tx position: RPR, Rx position: L_1, and $n_P = 0$.

The first step for extracting the S-V parameters is detection of clusters which is achieved by grouping the MPCs in the discrete PDP. Unfortunately the method is ambiguous and the available algorithms (see [19] and references therein) yield results that are very different from each other. This occurs due to manual setting of various thresholds. Our aim, however, is not to resolve this ambiguity; rather we consider a simple algorithm [61] for cluster detection and show (see Fig. 12) that the algorithm provide similar cluster profiles for the measured and simulated data sets.

Fig. 12 also exhibits the extraction of inter- and intra-cluster exponential decay rates. In the dB scale, the exponential decays appear as linear decrement. The cluster decay rate is calculated through the formula, $\Gamma = -10 \times \log_{10}(e)/\Delta_{\mathrm{PDP}}$, where Δ_{PDP} is the slope of the linear least squares fitting line passing through the maximum MPC of each cluster. The lines are indicated with black dashes. For deriving the ray decay rate (γ), such a linear fitting is applied to rays within each individual cluster, and are marked with red solid lines. The overall decay rate is computed by averaging the values over all identified clusters. In comparison, retrieving cluster arrival rate (Λ) and ray arrival rate (λ) are straightforward and involve only simple averaging of cluster duration and inter-MPC time, respectively.

TABLE V
COMPARISON OF AVERAGE S-V MODEL PARAMETERS FOR LOS SCENARIO

Parameter (ns)	Measured	Simulated	Liu [20]	CM 1 802.15.3a	CM 7 802.15.4a
Γ	10.74	11.15	7.20	7.1	13.47
γ	5.69	6.60	2.05	4.3	NA
$1/\Lambda$	8.27	8.87	3.80	42.92	14.10
$1/\lambda$	0.54	0.48	0.92	0.4	NA

In Table V we enlist all the four S-V parameter values averaged over the different LoS measurements performed in an empty car. The most important observation is that the measured values are in good agreement with the simulated values. The values obtained for a similar in-vehicle LoS scenario [20] cannot be directly compared due to the ambiguity in cluster identification. We also exclude values from [17], [21] as the authors conducted measurements in engine compartment and under the chasis instead of the passenger cabin. Parameter values for channel model 1 (CM 1) corresponds to indoor UWB propagation in the range 0-4 m as specified in IEEE standard 802.15.3a. On the other hand, CM 7 is specified in IEEE standard 802.15.4a for characterizing indoor industrial environment in the range 2-8 m.

VI. CONCLUSIONS

The key finding of the paper is, the transfer function of an intra-vehicle UWB channel can be modelled with an AR process after removing the frequency dependent trend. We have developed a comprehensive simulation framework for estimating both long term and short term frequency transfer function variations. Simulated transfer functions exhibit close match with the measured values. The similarity of coherence BWs, PDPs, RMS delay spreads, and S-V model parameters further validates the model.

REFERENCES

[1] G. Karagiannis, O. Altintas, E. Ekici, G. Heijenk, B. Jarupan, K. Lin, and T. Weil, "Vehicular networking: A survey and tutorial on requirements, architectures, challenges, standards and solutions," *IEEE Commun. Surveys Tuts.*, vol. 13, no. 4, pp. 584–616, Nov. 2011.

[2] J. Rybicki, B. Scheuermann, M. Koegel, and M. Mauve, "PeerTIS: A peer-to-peer traffic information system," in *Proc. ACM VANET*, Sep. 2009, pp. 23–32.

[3] O. Altintas, F. Dressler, F. Hagenauer, M. Matsumoto, M. Sepulcre, and C. Sommer, "Making cars a main ICT resource in smart cities," in *Proc. IEEE INFOCOM*, Apr. 2015, pp. 582–587.

[4] L. Delgrossi and T. Zhang, *Vehicle Safety Communications: Protocols, Security, and Privacy*. New Jersey, USA: John Wiley & Sons, Nov. 2012.

[5] IEEE Computer Society, "IEEE Standard for Information Technology - Telecommunications and information exchange between systems - Local and metropolitan area networks - Specific Requirements, Part 11: Wireless LAN Medium Access Control (MAC) and Physical Layer (PHY) Specifications, Amendment 6: Wireless Access in Vehicular Environments," IEEE Standard 802.11p, Jul. 2010.

[6] P. Kukolev, A. Chandra, T. Mikulásek, A. Prokeš, T. Zemen, and C. Mecklenbräuker, "In-vehicle channel sounding in the 5.8 GHz band," *EURASIP J. Wireless Commun. Netw.*, vol. 2015, no. 57, pp. 1–9, Mar. 2015.

[7] L. Zhu, F. R. Yu, B. Ning, and T. Tang, "Cross-layer design for video transmissions in metro passenger information systems," *IEEE Trans. Veh. Technol.*, vol. 60, no. 3, pp. 1171–1181, Mar. 2011.

[8] A. Chandra, J. Blumenstein, T. Mikulásek, J. Vychodil, R. Maršálek, A. Prokeš, T. Zemen, and C. Mecklenbräuker, "Serial subtractive deconvolution algorithms for time-domain ultra wide band in-vehicle channel sounding," *IET Intell. Transp. Syst.*, vol. 9, no. 9, pp. 870–880, Nov. 2015.

[9] S. Abdelhamid, H. Hassanein, and G. Takahara, "Vehicle as a resource (VaaR)," *IEEE Netw.*, vol. 29, no. 1, pp. 12–17, Jan. 2015.

[10] E. Costa-Montenegro, F. Quiñoy-García, and F. González-Castaño, F. J. Gil-Castiñeira, "Vehicular entertainment systems: Mobile application enhancement in networked infrastructures," *IEEE Veh. Technol. Mag.*, vol. 7, no. 3, pp. 73–79, Sep. 2012.

[11] P. Galdia, C. Koch, and A. Georgiadis, "Localization of passengers inside intelligent vehicles by the use of ultra wideband radars," in *Proc. SIP*, Dec. 2011, pp. 92–102.

[12] N. Nguyen, S. Dhakal, and J. Womack, "Localization of handheld devices inside vehicles using audio masking," in *Proc. ICCVE*, Dec. 2013, pp. 38–42.

[13] P. Pagani, F. T. Talom, P. Pajusco, and B. Uguen, *Ultra Wide Band Radio Propagation Channel*. Hoboken, NJ, USA: John Wiley & Sons, Mar. 2013.

[14] A. F. Molisch, R. F. Jeffrey, and P. Marcus, "Channel models for ultrawideband personal area networks," *IEEE Wireless Commun.*, vol. 10, no. 6, pp. 14–21, Dec. 2003.

[15] X. Wang, E. Anderson, P. Steenkiste, and F. Bai, "Improving the accuracy of environment-specific channel modeling," *IEEE Trans. Mobile Comput.*, pp. 1–15, 2016, In press. DOI: 10.1109/TMC.2015.2424426.

[16] I. G. Zuazola, J. M. Elmirghani, and J. C. Batchelor, "High-speed ultra-wide band in-car wireless channel measurements," *IET Commun.*, vol. 3, no. 7, pp. 1115–1123, Jul. 2009.

[17] W. Niu, J. Li, and T. Talty, "Ultra-wideband channel modeling for intravehicle environment," *EURASIP J. Wireless Commun. Netw.*, vol. 2009, no. 806209, pp. 1–12, Feb. 2009.

[18] P. C. Richardson, W. Xiang, and W. Stark, "Modeling of ultra-wideband channels within vehicles," *IEEE J. Sel. Areas Commun.*, vol. 24, no. 4, pp. 906–912, Apr. 2006.

[19] B. Li, C. Zhao, H. Zhang, X. Sun, and Z. Zhou, "Characterization on clustered propagations of UWB sensors in vehicle cabin: measurement, modeling and evaluation," *IEEE Sensors J.*, vol. 13, no. 4, pp. 1288–1300, Apr. 2013.

[20] L. Liu, Y. Wang, and Y. Zhang, "Ultrawideband channel measurement and modeling for the future intra-vehicle communications," *Microw. Opt. Technol. Lett.*, vol. 54, no. 2, pp. 322–326, Feb. 2012.

[21] W. Niu, J. Li, and T. Talty, "Intra-vehicle UWB channel measurements and statistical analysis," in *Proc. IEEE GLOBECOM*, Nov. 2008, pp. 1–5.

[22] A. A. Saleh and R. Valenzuela, "A statistical model for indoor multipath propagation," *IEEE J. Sel. Areas Commun.*, vol. 5, no. 2, pp. 128–137, Feb. 1987.

[23] O. Fernandez, L. Valle, M. Domingo, and R. P. Torres, "Flexible rays," *IEEE Veh. Technol. Mag.*, vol. 3, no. 1, pp. 18–27, Mar. 2008.

[24] T. Pedersen, G. Steinböck, and B. H. Fleury, "Modeling of reverberant radio channels using propagation graphs," *IEEE Trans. Antennas Propag.*, vol. 60, no. 12, pp. 5978–5988, Dec. 2012.

[25] J. Chuang, N. Xin, H. Huang, S. Chiu, and D. G. Michelson, "UWB radiowave propagation within the passenger cabin of a Boeing 737-200 aircraft," in *Proc. IEEE VTC*, Apr. 2007, pp. 496–500.

[26] M. Schack, J. Jemai, R. Piesiewicz, R. Geise, I. Schmidt, and T. Kürner, "Measurements and analysis of an in-car UWB channel," in *Proc. IEEE VTC*, May 2008, pp. 459–463.

[27] E. R. Bastidas-Puga, F. Ramírez-Mireles, and D. Muñoz-Rodríguez, "On fading margin in ultrawideband communications over multipath channels," *IEEE Trans. Broadcast.*, vol. 51, no. 3, pp. 366–370, Sep. 2005.

[28] W. Turin, *Performance Analysis and Modeling of Digital Transmission Systems*. New York, USA: Springer Science & Business Media, 2012.

[29] T. Taniguchi, A. Maeda, and T. Kobayashi, "Development of an omnidirectional and low-VSWR ultra wideband antenna," *Int. J. Wireless Opt. Commun.*, vol. 3, no. 2, pp. 145–157, Aug. 2006.

[30] J. S. McLean, R. Sutton, A. Medina, H. Foltz, and J. Li, "The experimental characterization of uwb antennas via frequency-domain measurements," *IEEE Antennas Propag. Mag.*, vol. 49, no. 6, pp. 192–202, Dec. 2007.

[31] J. Blumenstein, A. Prokes, T. Mikulasek, R. Marsalek, T. Zemen, and C. Mecklenbrauker, "Measurements of ultra wide band in-vehicle channel - statistical description and TOA positioning feasibility study," *EURASIP J. Wireless Commun. Netw.*, vol. 2015, no. 104, pp. 1–9, Apr. 2015.

[32] A. Prokeš, T. Mikulásek, J. Blumenstein, C. Mecklenbräuker, and T. Zemen, "Intra-vehicle ranging in ultra-wide and millimeter wave bands," in *Proc. IEEE APWiMob*, Aug. 2015, pp. 246–250.

[33] A. F. Molisch, K. Balakrishnan, D. Cassioli, C. C. Chong, S. Emami, A. Fort, J. Karedal, J. Kunisch, H. Schantz, and K. Siwiak, "A comprehensive model for ultrawideband propagation channels," in *Proc. IEEE GLOBECOM*, vol. 6, Nov. 2005, pp. 3648–3653.

[34] R. C. Qiu and I. T. Lu, "Wideband wireless multipath channel modeling with path frequency dependence," in *Proc. IEEE ICC*, vol. 1, Jun. 1996, pp. 277–281.

[35] ——, "Multipath resolving with frequency dependence for broadband wireless channel modeling," *IEEE Trans. Veh. Technol.*, vol. 48, no. 1, pp. 273–285, Jan. 1999.

[36] W. Q. Malik, D. J. Edwards, and C. J. Stevens, "Frequency-dependent pathloss in the ultrawideband indoor channel," in *Proc. IEEE ICC*, vol. 12, Jun. 2006, pp. 5546–5551.

[37] J. Kunisch and J. Pamp, "Measurement results and modeling aspects for the UWB radio channel," in *Proc. IEEE UWBST*, vol. 1, May 2002, pp. 19–23.

[38] A. Álvarez, G. Valera, M. Lobeira, R. P. Torres, and J. L. C. García, "New channel impulse response model for UWB indoor system simulations," in *Proc. IEEE VTC*, vol. 1, Apr. 2003, pp. 1–5.

[39] A. Chandra, P. Kukolev, T. Mikulásek, and A. Prokeš, "Autoregressive model of channel transfer function for UWB link inside a passenger car," in *Proc. CSCC*, Jul. 2015, pp. 238–241.

[40] A. F. Molisch, K. Balakrishnan, D. Cassioli, C. C. Chong, S. Emami, A. Fort, J. Karedal, J. Kunisch, H. Schantz, U. Schuster, and K. Siwiak, "IEEE 802.15.4a channel model - final report," Technical Report Document IEEE 802.15-04-0662-02-004a, 2005.

[41] S. S. Ghassemzadeh, R. Jana, C. W. Rice, W. Turin, and V. Tarokh, "Measurement and modeling of an ultra-wide bandwidth indoor channel," *IEEE Trans. Commun.*, vol. 52, no. 10, pp. 1786–1796, Oct. 2004.

[42] N. Alsindi, B. Alavi, and K. Pahlavan, "Empirical pathloss model for indoor geolocation using UWB measurements," *Electron. Lett.*, vol. 43, no. 7, pp. 370–372, Mar. 2007.

[43] C. C. Chong, Y. E. Kim, S. K. Yong, and S. S. Lee, "Statistical characterization of the UWB propagation channel in indoor residential environment," *Wireless Commun. Mobile Comput.*, vol. 5, no. 5, pp. 503–512, Aug. 2005.

[44] T. Kobayashi, "Measurements and characterization of ultra wideband propagation channels in a passenger-car compartment," in *Proc. IEEE ISSSTA*, Aug. 2006, pp. 228–232.

[45] C. U. Bas and S. C. Ergen, "Ultra-wideband channel model for intravehicular wireless sensor networks beneath the chassis: from statistical model to simulations," *IEEE Trans. Veh. Technol.*, vol. 62, no. 1, pp. 14–25, Jan. 2013.

[46] Y. H. Kim and S. C. Kim, "The effect of human bodies on path loss model in an indoor LOS environment," in *Proc. ICWMC*, Jul. 2013, pp. 152–156.

[47] M. Pecoraro, J. Venkataraman, G. Tsouri, and S. Dianat, "Characterization of the effects of the human head on communication with implanted antennas," in *Proc. IEEE APSURSI*, Jul. 2010, pp. 1–4.

[48] W. A. Woodward, H. L. Gray, and A. C. Elliott, *Applied Time Series Analysis*. Boca Raton, FL, USA: CRC Press, 2012.

[49] S. J. Howard and K. Pahlavan, "Autoregressive modeling of wide-band indoor radio propagation," *IEEE Trans. Commun.*, vol. 40, no. 9, pp. 1540–1552, Sep. 1992.

[50] A. Chehri and P. Fortier, "Frequency domain analysis of UWB channel propagation in underground mines," in *Proc. IEEE VTC*, Sep. 2006, pp. 1–5.

[51] F. Castanié, *Spectral Analysis: Parametric and Non-parametric Digital Methods*. NJ, USA: John Wiley & Sons, 2013.

[52] H. Akaike, "Use of statistical models for time series analysis," in *Proc. IEEE ICASSP*, vol. 11, Apr. 1986, pp. 3147–3155.

[53] B. Aksasse and L. Radouane, "Two-dimensional autoregressive (2-D AR) model order estimation," *IEEE Trans. Signal Process.*, vol. 47, no. 7, pp. 2072–2077, Jul. 1999.

[54] A. Taparugssanagorn, L. Hentilä, and S. Karhu, "Time-varying autoregressive process for ultra-wideband indoor channel model," in *Proc. IST Mobile Wireless Commun. Summit*, Jun. 2005, pp. 1–5.

[55] G. Morrison, M. Fattouche, and H. Zaghloul, "Statistical analysis and autoregressive modeling of the indoor radio propagation channel," in *Proc. IEEE ICUPC*, Sep. 1992, pp. 97–101.

[56] I. Cuiñas and M. G. Sánchez, "Measuring, modeling, and characterizing of indoor radio channel at 5.8 GHz," *IEEE Trans. Veh. Technol.*, vol. 50, no. 2, pp. 526–535, Mar. 2001.

[57] D. Scammell, A. Hammoudeh, and M. G. Sánchez, "Estimating channel performance for time invariant channels," *Electron. Lett.*, vol. 40, no. 12, pp. 746–747, Jun. 2004.

[58] M. Ghaddar, L. Talbi, and G. Y. Delisle, "Coherence bandwidth measurement in indoor broadband propagation channel at unlicensed 60 GHz band," *Electron. Lett.*, vol. 48, no. 13, pp. 795–797, Jun. 2012.

[59] A. Chandra, P. Kukolev, T. Mikulásek, and A. Prokeš, "Frequency-domain in-vehicle channel modelling in mmW band," in *Proc. IEEE RTSI*, Sep. 2015, pp. 106–110.

[60] A. Chandra, J. Blumenstein, T. Mikulásek, J. Vychodil, M. Pospísil, R. Maršálek, A. Prokeš, T. Zemen, and C. Mecklenbräuker, "CLEAN algorithms for intra-vehicular time-domain UWB channel sounding," in *Proc. PECCS*, Feb. 2015, pp. 224–229.

[61] M. Corrigan, A. Walton, W. Niu, J. Li, and T. Talty, "Automatic UWB clusters identification," in *Proc. IEEE RWS*, Jan. 2009, pp. 376–379.

Aniruddha Chandra (M'08) received B.E., M.E., and Ph.D. degrees from Jadavpur University, Kolkata, India in 2003, 2005, and 2011 respectively.

He joined Electronics and Communication Engineering department, National Institute of Technology, Durgapur, India in 2005 as a Lecturer. He is currently serving as an Assistant Professor there. From August 2011 to January 2012 he was a visiting Assistant Professor at Asian Institute of Technology, Bangkok. In 2014, he received Marie Curie fellowship to pursue postdoctoral studies in Brno University of Technology, Czech Republic.

Dr. Chandra published about 80 research papers in referred journals and peer-reviewed conferences. He has also delivered several invited lectures. His primary area of research is physical layer issues in wireless communication.

Aleš Prokeš graduated from the Brno University of Technology (BUT) in 1988. Since 1990 he is with the Faculty of Electrical Engineering and Communication (FEEC), BUT. He received Ph.D degree in the field of generalized sampling theorem applications in 1999 and in 2006 he habilitated and became an Associate Professor. Currently he is serving as a Professor at BUT.

He has (co)authored 8 internal textbooks, over 120 publications and conducted several FRVS (Development Fund of Czech Universities) and GACR (Grant Agency of the Czech Republic) projects.

His research interests include signal processing in communication systems, nonuniform sampling and signal reconstruction, velocity measurement based on spatial filtering, beam propagation in atmosphere and optical receivers and transmitters for free-space optical communications.

Pavel Kukolev received his Masters degree in electrical engineering at the Izhevsk State Technical University in Izhevsk, Russia in 2009. At present, he is a Ph.D. student at the Department of Radio Electronics, Brno University of Technology.

His research interests are focused to wireless communication.

Tomáš Mikulášek received his Bachelor's, Masters, and Ph.D. degree from Brno University of Technology in 2007, 2009, and 2013, respectively. In 2012 he worked at the Centre Tecnológic Telecomunicacions Catalunya (CTTC), Barcelona, Spain. At present, he is a researcher at the Department of Radio Electronics, Brno University of Technology.

His research interests include analysis and design of antennas, modeling and simulation of microwave and RF structures, and antenna measurement.

Thomas Zemen (S'03-M'05-SM'10) received the Dipl.-Ing. degree (with distinction) in electrical engineering in 1998, the Ph.D. degree (with distinction) in 2004 and the Venia Docendi (Habilitation) for "Mobile Communications" in 2013, all from Vienna University of Technology, Vienna, Austria.

Since 2014 Thomas Zemen has been Senior Scientist at AIT Austrian Institute of Technology. From 2003 to 2014 he was with FTW Forschungszentrum Telekommunikation Wien and Head of the "Signal and Information Processing" department since 2008. From 1998 to 2003 Thomas Zemen worked as Hardware Engineer and Project Manager for the Radio Communication Devices Department, Siemens Austria.

He is the author or coauthor of 4 book chapters, 23 journal papers and more than 70 conference communications. His research interests focuses on ultra-reliable, low-latency wireless machine-to-machine communications for sensor and actuator networks, vehicular channel measurements and modeling, time-variant channel estimation, cooperative communication systems and interference management.

Dr. Zemen is docent at the Vienna University of Technology and serves as Associate Editor for the IEEE Transactions on Wireless Communications.

Christoph F. Mecklenbräuker (S'88-M'97-SM'08) received the Dipl.-Ing. degree in electrical engineering from the Technische Universität Wien, Vienna, Austria, in 1992 and the Dr.-Ing. degree from the Ruhr-Universität Bochum, Bochum, Germany, in 1998, both with distinction. His doctoral dissertation on matched field processing received the Gert-Massenberg Prize in 1998.

From 1997-2000, he worked for the Mobile Networks Radio department of Siemens AG Austria where he participated in the European framework of ACTS 90 FRAMES. He was a delegate to the Third Generation Partnership Project (3GPP) and engaged in the standardisation of the radio access network for UMTS. From 2000 to 2006, he has held a senior research position with the Telecommunications Research Center Vienna (FTW), Vienna, in the field of mobile communications. In 2006, he joined the Institute of Communications and Radio Frequency Engineering at Vienna University of Technology as a full professor. Since July 2009, he leads the newly founded Christian Doppler Laboratory for Wireless Technologies for Sustainable Mobility.

He has authored approximately 100 papers in international journals and conferences, for which he has also served as a reviewer, and holds eight patents in the field of mobile cellular networks. His current research interests include radio interfaces for future peer-to-peer networks (car-to-car communications, personal area networks, and wireless sensor networks), ultra-wideband radio (UWB) and MIMO-OFDM based transceivers (UMTS long term evolution, WiMax, and 4G).

Dr. Mecklenbräuker is a member of the IEEE, the Antennas and Propagation Society, the Vehicular Technology society, the Signal Processing society, as well as VDE and EURASIP. He is the councilor of the IEEE Student Branch Wien. He is associate editor of the EURASIP Journal of Applied Signal Processing.